

Article

WAAM Technique: Process Parameters Affecting the Mechanical Properties and Microstructures of Low-Carbon Steel

Van-Thuc Nguyen ^{1,*}, Pham Son Minh ^{1,*} , Tran Minh The Uyen ¹, Thanh Trung Do ¹ , Han Vuong Thi Ngoc ¹, Minh-Tai Le ¹  and Van Thanh Tien Nguyen ^{2,3,*}

- ¹ HCMC University of Technology and Education, Ho Chi Minh City 71307, Vietnam; uyentmt@hcmute.edu.vn (T.M.T.U.); trungdt@hcmute.edu.vn (T.T.D.); hanvtn@hcmute.edu.vn (H.V.T.N.); tailm@hcmute.edu.vn (M.-T.L.)
- ² Department of Industrial Engineering and Management, National Kaohsiung University of Science and Technology, Kaohsiung 80778, Taiwan
- ³ Faculty of Mechanical Engineering, Industrial University of Ho Chi Minh City, Nguyen Van Bao Street, Ward 4, Go Vap District, Ho Chi Minh City 70000, Vietnam
- * Correspondence: nvthuc@hcmute.edu.vn (V.-T.N.); minhps@hcmute.edu.vn (P.S.M.); i110143109@nkust.edu.tw (V.T.T.N.)

Abstract: This study surveys the influences of travel speed, voltage, and intensity on the characteristics of low-carbon steel samples generated by the Wire Arc Additive Manufacturing (WAAM) technique. The results indicated that the WAAM samples have isotropy grain shape, with grain size number values varying from about 8 to 12. Interestingly, the WAAM sample achieves better mechanical properties with a higher ultimate tensile strength (UTS) value and higher elongation at break value than the original wire. The UTS value of the WAAM sample is 21–40% higher than the original steel wire. The WAAM sample with a travel rate of 350 mm·min⁻¹, a voltage of 24 V, and an electrical intensity of 120 A reaches the highest UTS value of 694 MPa. The WAAM sample with a travel rate of 400 mm·min⁻¹, a voltage of 22 V, and an electrical intensity of 170 A gains the lowest UTS value of 599 MPa. Moreover, the elongation values oscillate around 41–57%, two or three times higher than the original steel wire. SEM microstructure reveals a ductile fracture surface with dimples of the samples after the tensile test, indicating the toughness of the samples. The fracture surface also shows the equiaxial shape and grain size of the WAAM samples. According to Taguchi analyses, the travel rate factor greatly impacts grain size. The voltage factor has the highest effect on the UTS value. The intensity factor has the most significant impact on the elongation value.

Keywords: additive manufacturing; 3D printing; microstructure; travel rate; voltage; intensity



Citation: Nguyen, V.-T.; Minh, P.S.; Uyen, T.M.T.; Do, T.T.; Ngoc, H.V.T.; Le, M.-T.; Tien Nguyen, V.T. WAAM Technique: Process Parameters Affecting the Mechanical Properties and Microstructures of Low-Carbon Steel. *Metals* **2023**, *13*, 873. <https://doi.org/10.3390/met13050873>

Academic Editors: Dongsheng Wu, Matteo Benedetti and Lei Hu

Received: 18 March 2023
Revised: 26 April 2023
Accepted: 28 April 2023
Published: 30 April 2023



Copyright: © 2023 by the authors. Licensee MDPI, Basel, Switzerland. This article is an open access article distributed under the terms and conditions of the Creative Commons Attribution (CC BY) license (<https://creativecommons.org/licenses/by/4.0/>).

1. Introduction

Recently, additive manufacturing (AM) has emerged as a promising manufacturing method that, in many cases, could replace traditional manufacturing methods [1–3]. The original material shapes for AM method are powder or wire, and they are melted and adhered to generate the designed forms. Powder materials require a laser beam or electron beam which are expensive and high-energy consumption devices, despite the fact that they could build high-resolution parts [4–7]. Compared to powder materials, wire shapes have the merits of saving fusion energy and time during the additive process. Significantly, the metal wire could create high mechanical characteristics that could be applied in marine, aerospace, and automobile industries [8–10].

Due to the availability of arc generation devices, the Wire Arc Additive Manufacturing (WAAM) technique has attracted much attention [11–15]. Additionally, wires in various sizes and material types can be easily found on the market. This method has the benefits of high productivity, low cost, industrial readiness, and the capacity to produce large numbers of products [16–20]. During the WAAM process, many factors, such as material

selection, travel rate, electrical voltage, and electrical intensity, are the main parameters that impact the sample quality. Prado-Cerqueira et al. [21] showed that with an AWS ER70S-6 steel wire, 0.8 mm diameter, the optimal travel rate should be $400 \text{ mm}\cdot\text{min}^{-1}$; increasing the travel rate over $400 \text{ mm}\cdot\text{min}^{-1}$ reduces the shape accuracy and surface quality. According to Wang et al. [22], the WAAM sample's tensile strength could be increased to 540 MPa by using 316L stainless steel wire at 22.1 A, 135 V, and $600 \text{ mm}\cdot\text{min}^{-1}$. In contrast, Lou et al. [23] examined how the arc mode affected the wire's 6061 aluminum alloy properties. They suggested that a small-power pulsed arc is preferable for increasing efficiency. Popov et al. [24] proved that the WAAM technique could achieve a deposition rate of $50\text{--}130 \text{ g}\cdot\text{min}^{-1}$, which is significantly higher than laser or electron beam techniques. In laser/electron beam techniques, the deposition rate can only reach $2\text{--}10 \text{ g}\cdot\text{min}^{-1}$. Besides the advantage of a high deposition rate, Evans et al. [25] pinpointed that the WAAM technique does not require a vacuum and a powder recycling system in contrast to a technique using powder. Martina et al. [26] applied the WAAM technique to fabricate a 3D printing component from a 17-4 pH stainless steel wire. The deposition rate was $9.5 \text{ kg}\cdot\text{h}^{-1}$, and the travel speed reached $1200 \text{ mm}\cdot\text{min}^{-1}$ when the printing was assisted with a tandem torch. Takagi et al. [27] used magnesium alloys to conduct WAAM components and indicated that the printed components had a lower rate of defects than conventional techniques. The tensile strength of the printed component was sufficient compared to the bulk materials. Interestingly, Shi et al. [28] designed an active cooling system consisting of a cooling well that removes excessive heat input during printing. The cooling system helped increase 9–15% wire-feed and reduced 42–54% dwell time.

Interestingly, Yildiz et al. [29] studied the WAAM process of high-strength low, alloy steel wire. This study pointed out that the orientation of the tensile specimen influences the tensile properties. The samples with horizontal direction are more substantial than the vertical ones. The tensile strength, yield strength, and elongation values of the horizontal direction are 509 MPa, 955 MPa, and 20.1%, while in the vertical direction, these values are 493 MPa, 934 MPa, and 17.4 MPa. Xiong et al. [30] stated that increasing the travel and wire feeding rates leads to an increase in surface roughness. Hosseini et al. [31] studied the effects of printing paths on the shape of the duplex stainless steel sample. Suitable printing paths could achieve uniform layer shapes. Feng et al. [32] surveyed the influence of single and double-wire feeding systems on the surface quality of the WAAM sample. They revealed that the double-wire feeding system could increase the printed sample's efficiency and surface quality. The summary of some previous WAAM studies is presented in Table 1. The WAAM process could become a manufacturing method that, in many cases, could replace conventional manufacturing methods. Wire shapes can save fusion energy and time during the additive process compared to powder materials. Significantly, the metal wire could create high mechanical characteristics that could be applied in the marine, aerospace, and automobile industries. Therefore, the Wire Arc Additive Manufacturing (WAAM) technique has attracted much attention. During the WAAM process, many factors, such as material selection, travel rate, electrical voltage, and electrical intensity and devices, impact the sample quality. Thus, this special issue focuses on the effects of parameters and devices on the characteristics of the WAAM sample. The characteristics of a popular mild steel wire such as AWS E70S-6 are rarely discussed.

In this study, we aim to investigate the effects of travel rate, electrical voltage, and electrical intensity on the microstructure and mechanical properties of the WAAM sample. The selected printing wire is AWS E70S-6. Remarkably, the sample is printed using a CNC machine and a conventional welding machine. The results could be easily applied in the industry as the printing wire and the equipment are available. Additionally, the study reveals the optimal parameters for achieving the desired mechanical properties and microstructure.

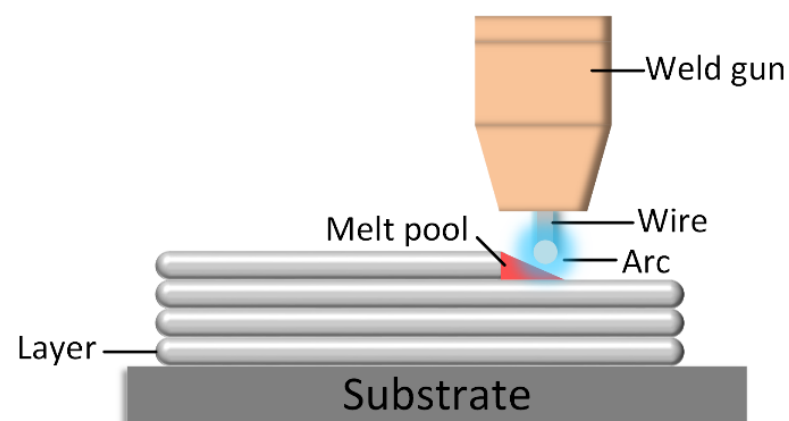
Table 1. Summary of some prior WAAM reports.

Materials	Process Parameters	Characteristics	References
AWS ER70S-6 steel wire	Increase travel rate	Reduce the shape accuracy and surface quality	Prado-Cerqueira et al. [21]
6061 aluminum alloy wire	Small-power pulsed arc	Increase efficiency	Lou et al. [23]
2325 aluminum alloy wire	Cooling rate with the active cooling system	Increase wire feeding rate and reduce dwell time	Shi et al. [28]
H08MnSi low-carbon steel wire	Increase travel rate, wire feeding rate	Surface roughness increase	Xiong et al. [30]
Duplex stainless steel	Deposition paths	Uniform layer shape	Hosseini et al. [31]
316L stainless steel wire	Single-wire and double-wire feed	Better surface quality	Feng et al. [32]

2. Experimental Methods

Figure 1 shows the typical WAAM process. The preparation process to generate a 3D printing steel sample is presented in Figure 2. Initially, the welding gun is fixed on a CNC machine. After that, the sample is printed on an S20C steel base to reduce the heat and avoid sample deformation. The composition of the S20C steel base is presented in Table 2. The steel wire used for this process is AWS A5.18 ER 70S-6 with a 0.8 mm diameter. The wire has a minimum tensile strength of 496 MPa and a 22% elongation value. The chemical composition of the AWS A5.18 ER 70S-6 steel wire is shown in Table 3. The sample shape is then created in accordance with ASTM E8/E8M-13 standards. After preliminary tests to eliminate some welding problems, the WAAM process parameters are set in Table 4. Each sample number has three samples, and three sample numbers create 01 sample group. The sample in the same group has the same voltage and intensity. Table 4 is built by some tests before conducting experiments. We also considered some previous studies that were mentioned in the introduction section. Moreover, the Minitab software also helps us design the experiment and analyze the results.

After printing, the block is cut into smaller samples by wire-cutting method. WAAM samples are analyzed via the microstructure and the mechanical properties. The samples are polished using the grinding polishing MP-2B machine and etched with Nital 4% solution before being examined for metallurgical microstructure. The microstructures are observed via optical and SEM microscopes (JEOL 5410 LV, Japan), and the mechanical properties are investigated by a tensile test machine (SANS model CHT4106, China). The mechanical analyses involve Minitab software with L8 orthogonal array, three factors, and two levels. The orthogonal array is relatively small but helps point out the affecting rate between different factors.

**Figure 1.** The mechanism of the WAAM process.

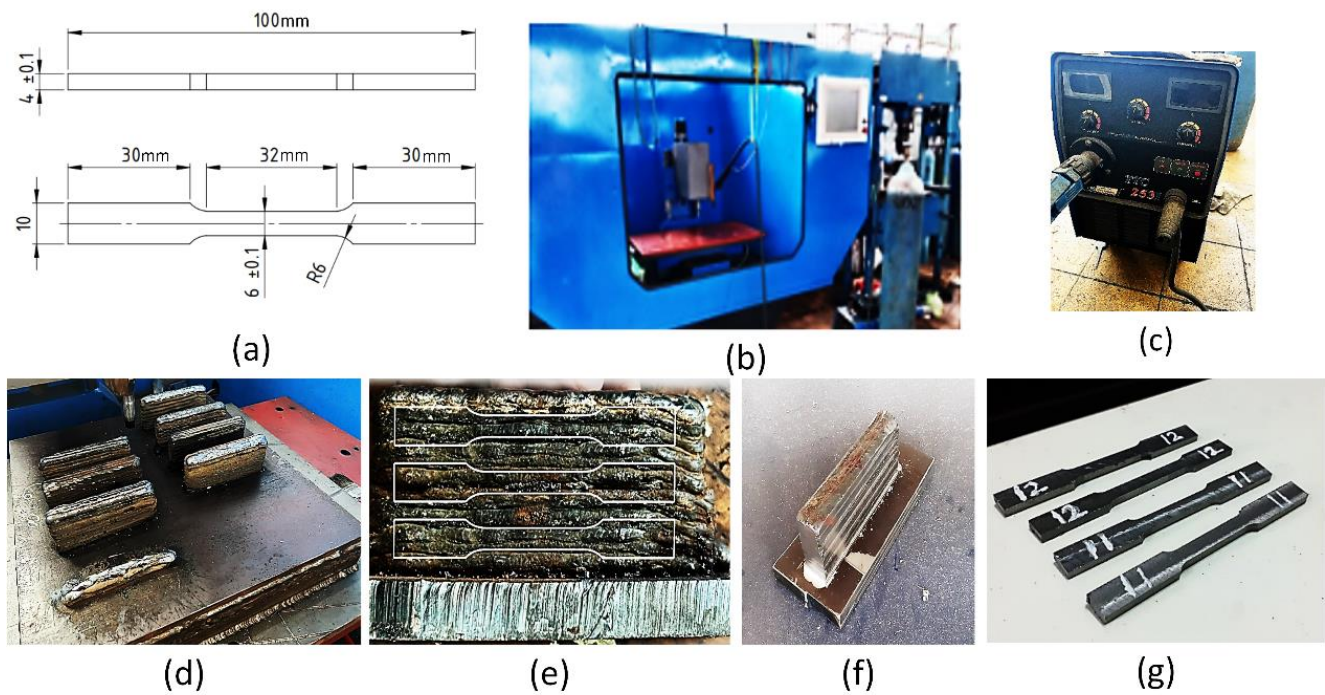


Figure 2. The WAAM equipment and samples: (a) sample size, (b) CNC machine, (c) welding machine MIG Tan Thanh TTC 253I, (d) steel base with printed samples, (e) sample block for cutting, (f) cut samples, and (g) sample for tensile test.

Table 2. Chemical composition of S20C steel base.

Weight %	C	Si	Mn	P	S	Ni	Cr	Cu
S20C	0.18–0.23	0.15–0.35	0.3–0.6	0.03 max	0.035 max	0.2 max	0.2 max	0.3 max

Table 3. Chemical composition of welding wire grade AWS A5.18 ER 70S-6.

Weight %	C	Mn	Si	P	S	Ni	Cr	Mo	V	Cu
ER 70S-6	0.06–0.15	1.40–1.85	0.80–1.15	0.025 max	0.035 max	0.15 max	0.15 max	0.15 max	0.03 max	0.05 max

Table 4. The WAAM process parameters of the experiment.

Sample		Travel Rate (mm·min ⁻¹)	Voltage (V)	Intensity (A)
1	Group 1	300	22	170
2		350	22	170
3		400	22	170
4	Group 2	300	24	170
5		350	24	170
6		400	24	170
7	Group 3	300	24	120
8		350	24	120
9		400	24	120
10	Group 4	300	22	120
11		350	22	120
12		400	22	120

3. Results and Discussion

3.1. Microstructure

Figure 3 shows the microstructures of the WAAM samples at different process parameters. The figure demonstrates that the microstructures comprise a pearlite phase that scatters on the ferrite matrix and a white ferrite phase, as shown in Figure 3h. These metallurgy microstructures show the low-carbon steel structure of the welding wire due to the dominant ferrite phase compared to the pearlite phase [33–35]. Furthermore, the grain shape of the samples has a better isotropy shape than the textured grain of welding wire, which has an anisotropy shape. The reason is that the melting and solidification during the WAAM process reshape the steel samples' grain size structure, eliminating the initial wire's original anisotropy shape. The grain sizes of different process parameters have a similar range, and more than the difference between these grain sizes is required. To further evaluate and compare the grain size of these samples, the grain size distribution is presented in the following result.

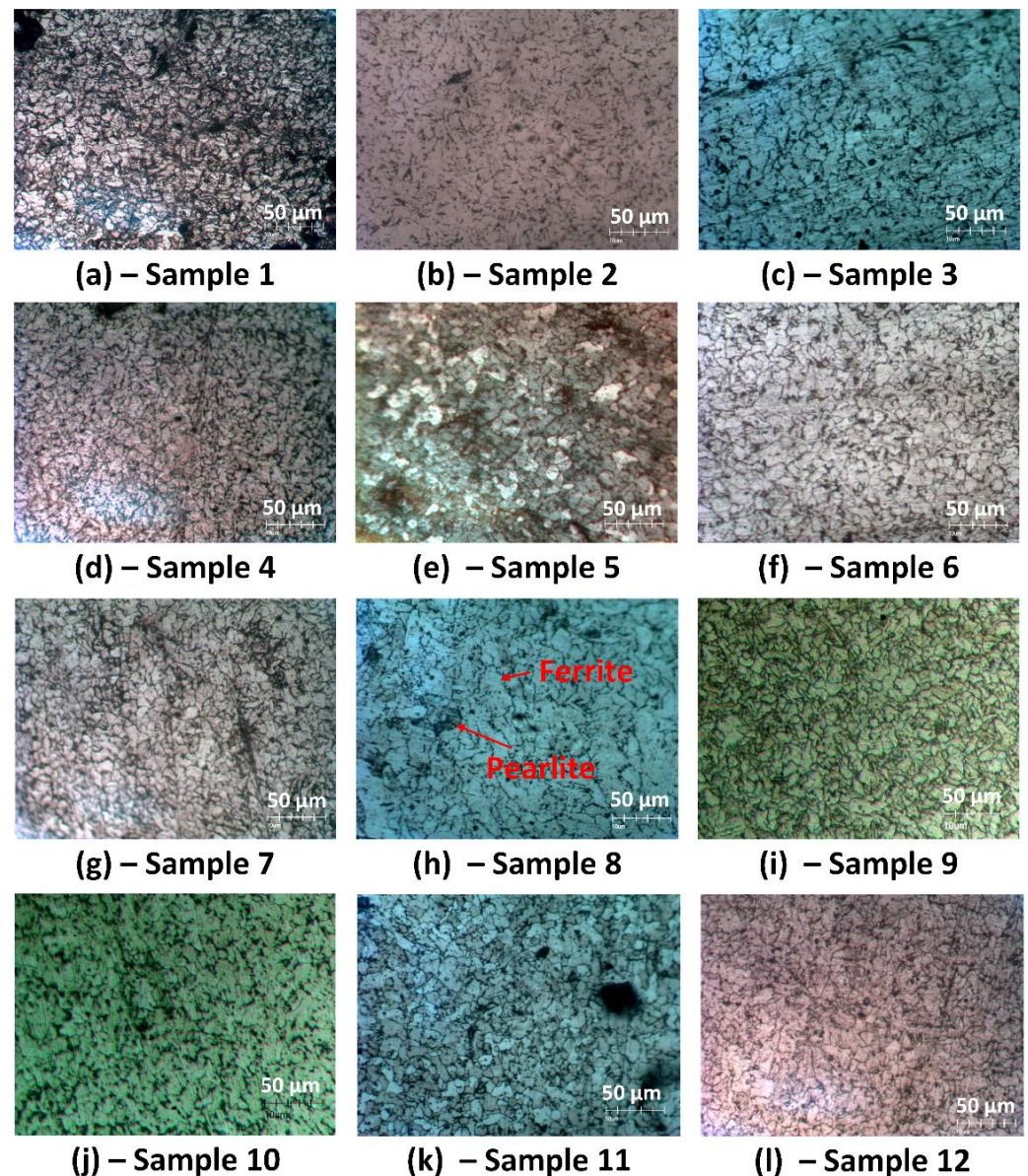


Figure 3. Microstructure of WAAM samples at different process parameters: (a) sample 1, (b) sample 2, (c) sample 3, (d) sample 4, (e) sample 5, (f) sample 6, (g) sample 7, (h) sample 8, (i) sample 9, (j) sample 10, (k) sample 11, and (l) sample 12.

Figure 4 shows the grain size number distribution of WAAM samples at different process parameters. The grain dimensions are measured via ImageJ software and classified using the ASTM E112 standard:

$$N\left(\frac{M}{100}\right)^2 = 2^{(n-1)} \quad (1)$$

where N is the number of grains per square inch, n is the grain size number, and M is the magnification. Before melting to form the WAAM sample, the original grain size number of the steel wire that suffered the cold drawing process varies from 11 to 12. Generally, the grain size numbers vary around 8–12, primarily concentrated in the 9–11 range. The average grain area values range from $62 \mu\text{m}^2$ to $207 \mu\text{m}^2$, as shown in Table 5. These results indicate that sample 5 with $F = 350 \text{ mm}\cdot\text{min}^{-1}$, $U = 24 \text{ V}$, and $I = 170 \text{ A}$ has the smallest grain size. On the other hand, sample 10 with $F = 300 \text{ mm}\cdot\text{min}^{-1}$, $U = 22 \text{ V}$, and $I = 120 \text{ A}$ has the largest grain size. Notably, with the same voltage of 22 V , sample group 1 with the intensity of 170 A has a smaller average grain size of $92 \mu\text{m}^2$ than other cases. In contrast, sample group 4, with the intensity of 120 A , has the largest average grain size with $134.3 \mu\text{m}^2$. Overall, the electrical intensity significantly impacts the sample grain size. A Taguchi analysis is conducted in the following results to compare these parameters' influence on the grain size.

Table 5. Average grain size area of WAAM samples at different process parameters.

Sample	1	2	3	4	5	6	7	8	9	10	11	12
Grain size (μm^2)	90	84	103	166	62	94	107	137	147	207	117	79

Table 6 presents the response table for Signal-to-Noise ratios for grain size, applying the criteria “smaller is better”. Factor travel rate recycled has levels of $300 \text{ mm}\cdot\text{min}^{-1}$ and $300 \text{ mm}\cdot\text{min}^{-1}$; factor voltage has levels of 22 V and 24 V ; factor intensity has levels of 120 V and 170 V . The results demonstrate that factor travel rate is the most impact factor of the grain size. The intensity rate has a lower influence rate, while the voltage factor has the lowest influence rate. Increased travel rate and intensity could lead to a smaller grain size, while increasing the voltage leads to more apparent grain size, as shown in Figure 5.

Table 6. Response table for Signal-to-Noise ratios for grain size (smaller is better).

Level	Travel Rate	Voltage	Intensity
1	−42.60	−40.90	−42.05
2	−40.25	−41.95	−40.80
Delta	2.34	1.05	1.25
Rank	1	3	2

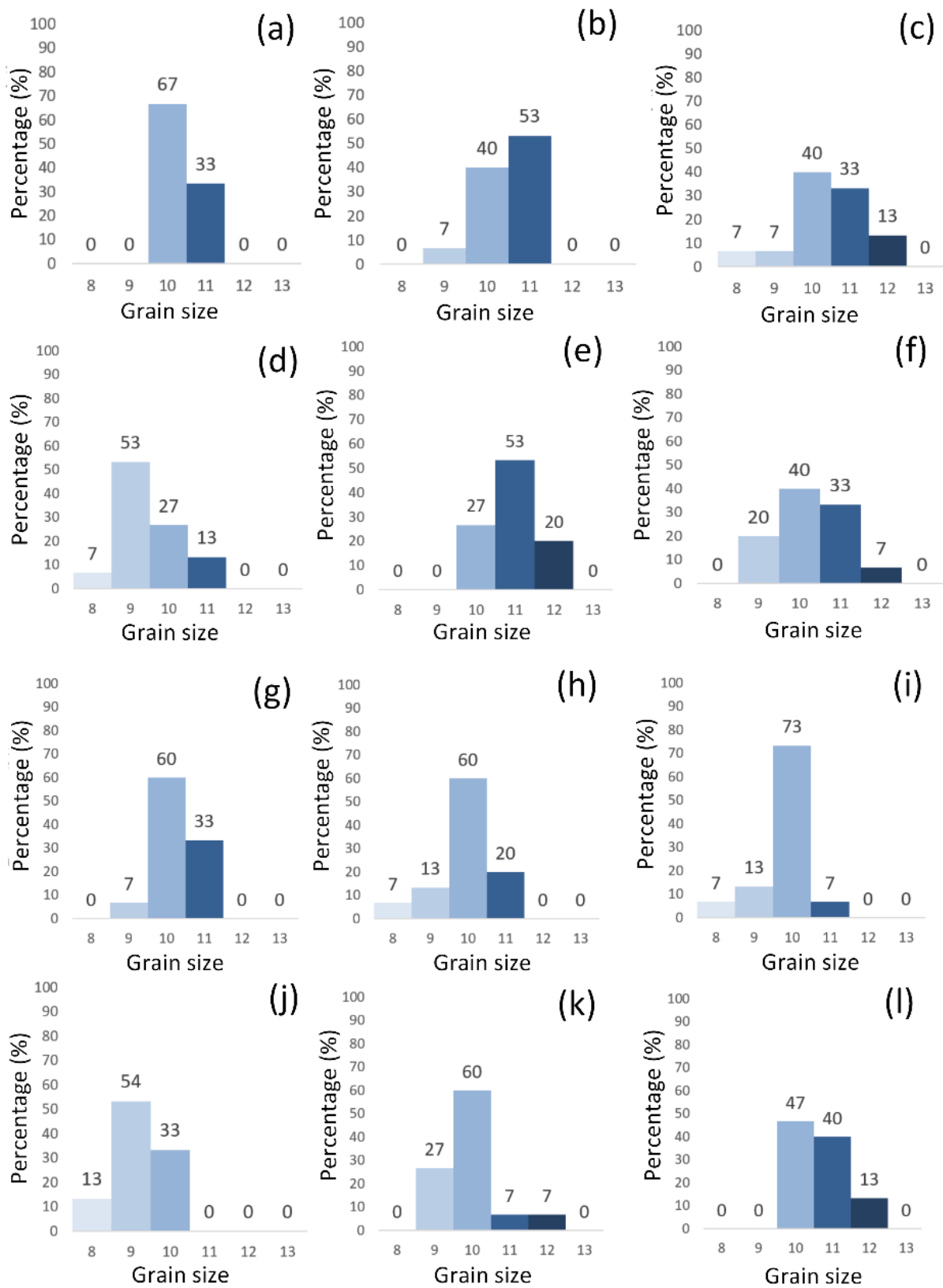


Figure 4. Grain size number distribution following ASTM E112-10 grain size number standard of WAAM samples at different process parameters: (a) sample 1, (b) sample 2, (c) sample 3, (d) sample 4, (e) sample 5, (f) sample 6, (g) sample 7, (h) sample 8, (i) sample 9, (j) sample 10, (k) sample 11, and (l) sample 12.

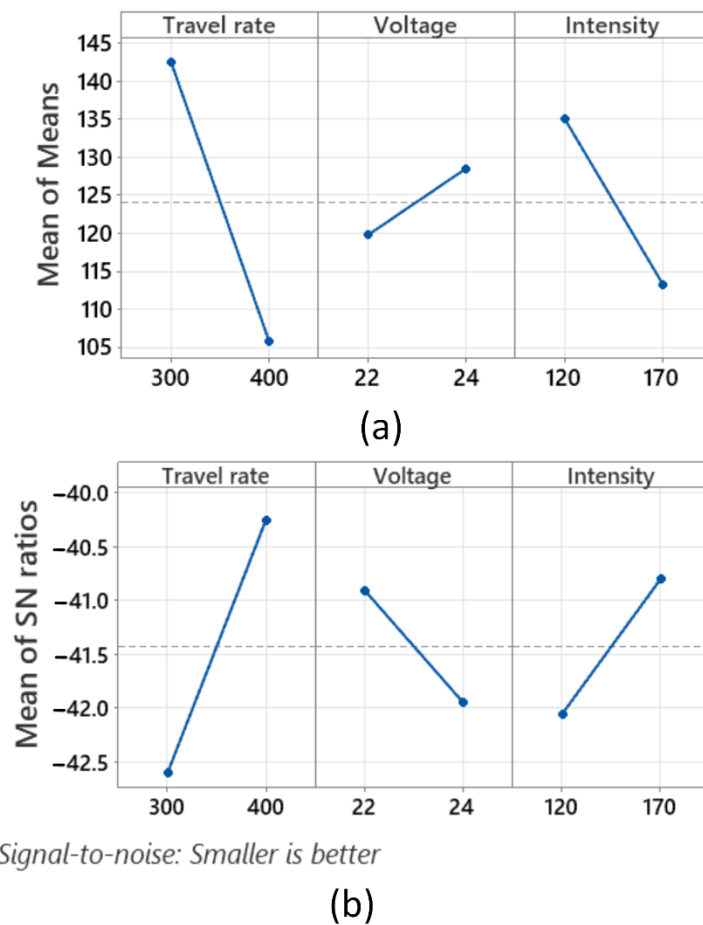


Figure 5. Taguchi analysis for grain size: (a) Main Effects Plot for Means, and (b) SN ratios for Signal-to-Noise ratios (smaller is better).

3.2. Tensile Strength

Figure 6 represents the stress-strain diagrams of the WAAM samples at different process parameters. Each sample number has three samples, and the average mechanical properties of the WAAM samples are shown in Table 7. The ultimate tensile strength (UTS) values range from 599 MPa to 694 MPa. Remarkably, compared to the original welding wire AWS A5.18 ER 70S-6, which possesses a UTS value of 496 MPa, the WAAM sample obtains a considerably higher UTS value. The UTS value of the WAAM sample is 21–40% higher than the original steel wire. The reason is the rapid melting and cooling rates during the printing process, leading to a fine microstructure of the WAAM sample [36]. In addition, sample 8 with $F = 350 \text{ mm} \cdot \text{min}^{-1}$, $U = 24 \text{ V}$, and $I = 120 \text{ A}$ reaches the highest UTS value of 694 MPa. On the contrary, sample 3 with $F = 400 \text{ mm} \cdot \text{min}^{-1}$, $U = 22 \text{ V}$, and $I = 170 \text{ A}$ gains the lowest UTS value of 599 MPa. Furthermore, compared to other travel rates, a $350 \text{ mm} \cdot \text{min}^{-1}$ travel rate creates higher UTS values than samples. In detail, when considering inside the small group 1–4 with the same voltage and ampere values, samples 2, 5, 8, and 11 with a travel rate of $350 \text{ mm} \cdot \text{min}^{-1}$ have higher UTS values. Furthermore, group 3 appears to obtain the highest average UTS value of 639 MPa, while group 4 has the lowest highest average UTS value of 639 MPa compared to other groups. The reason for the yield strength value of sample 4 could be explained by the Hall–Petch equation, in which a larger grain size leads to a lower strength. Sample 4, with a grain size of $166 \mu\text{m}^2$, which is the large grain size, has very low UTS values of 602 MPa. On the contrary, samples 5 and 12 have high yield strengths of 518 MPa and 521 MPa due to the small grain size of $62 \mu\text{m}^2$ and $79 \mu\text{m}^2$.

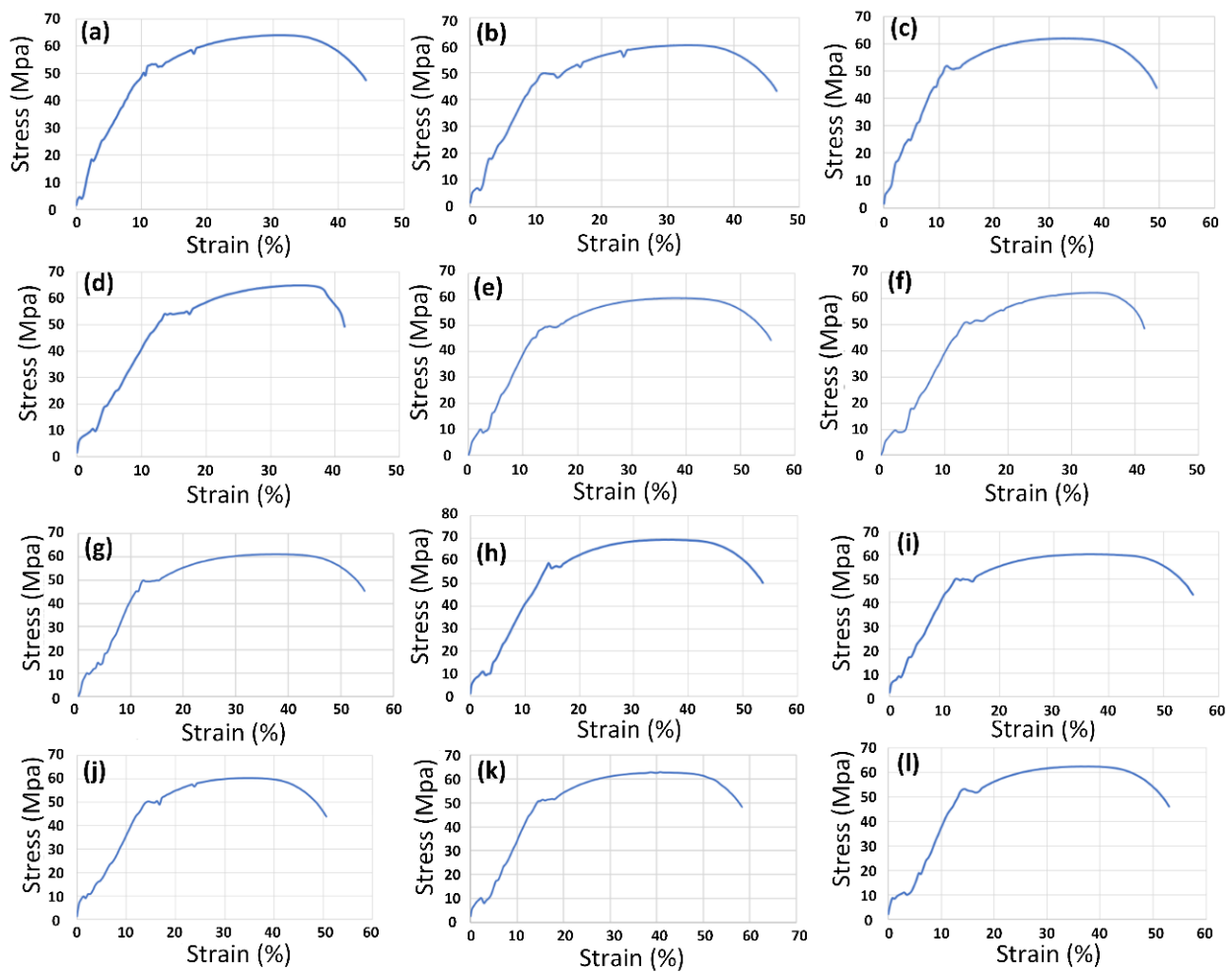


Figure 6. Stress-strain diagrams of WAAM samples at different process parameters: (a) sample 1, (b) sample 2, (c) sample 3, (d) sample 4, (e) sample 5, (f) sample 6, (g) sample 7, (h) sample 8, (i) sample 9, (j) sample 10, (k) sample 11, and (l) sample 12.

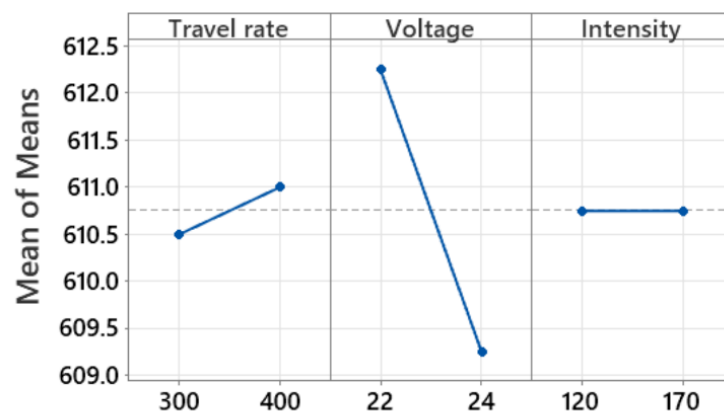
Table 7. Average mechanical properties of the WAAM samples at different process parameters.

Sample	Yield Strength (MPa)	UTS (MPa)	Elongation at Break (%)
1	519	631	48 41
2	509	625	41
3	492	599	41
4	495	602	52
5	518	626	41
6	499	611	54
7	496	608	56
8	590	694	46
9	514	616	56
10	512	601	55
11	511	618	57
12	521	618	54

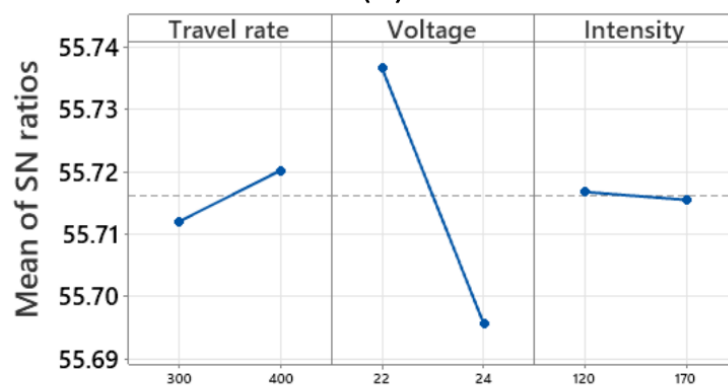
The response table for Signal-to-Noise ratios for UTS values using the maxim “larger is better” is shown in Table 8. The UTS value is most significantly impacted by factor voltage and the travel rate has a lower influence rate, while the intensity factor has the lowest influence rate. Unlike the grain size response, where the voltage factor is the most negligible impact factor, the voltage factor is now the most impact factor on the UTS value. Figure 7 demonstrates that while the intensity has little effect on the UTS value, a higher travel rate and a lower voltage may result in a higher UTS value.

Table 8. Response table for Signal-to-Noise ratios for UTS value (larger is better).

Level	Travel Rate	Voltage	Intensity
1	55.71	55.74	55.72
2	55.72	55.70	55.72
Delta	0.01	0.04	0.00
Rank	2	1	3



(a)



Signal-to-noise: Larger is better

(b)

Figure 7. Taguchi analysis for UTS value: (a) Main Effects Plot for Means, and (b) SN ratios for Signal-to-Noise ratios (larger is better).

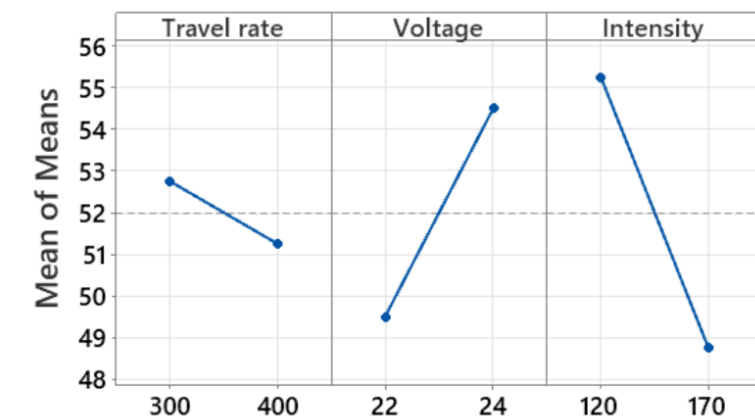
Table 7 shows the elongation of WAAM samples at different process parameters. Interestingly, compared to the original welding wire AWS A5.18 ER 70S-6, which has an elongation of 22%, the WAAM sample obtains an exceedingly higher elongation value. The elongation values oscillate around 41–57%, two or three times higher than the original wire. The reason for this significant improvement may be the same as the reason for the

increase in UTS value. The macrostructure of the printing pathway leads to an increase in the ductility of the sample. Moreover, samples 10, 11, and 12 with low voltage and intensity ($U = 22\text{ V}$, $I = 120\text{ A}$) present high elongation values of 55%, 57%, and 54%. On the contrary, samples 1, 2, and 3 with higher intensity ($U = 22\text{ V}$, $I = 170\text{ A}$) represent high elongation values of 48%, 41%, and 41%.

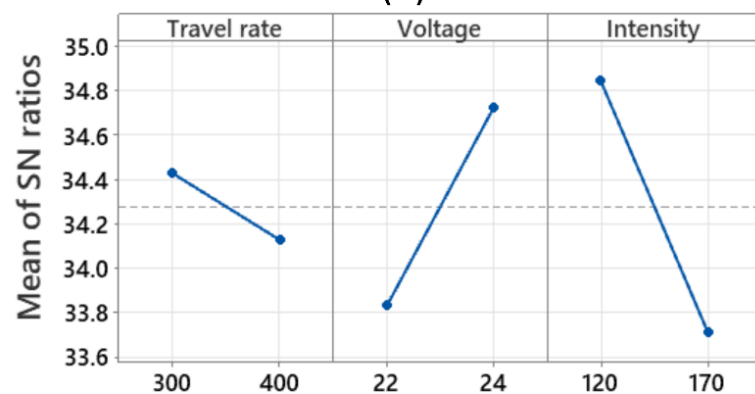
Table 9 shows the response table for Signal-to-Noise ratios for elongation values using the “larger is better” criterion; factor intensity significantly influences the elongation value. Voltage has the lowest influence rate, while the travel rate factor has the lowest. In contrast to the UTS value response where the intensity factor has the most negligible impact, the intensity factor now has the most significant effect on the elongation value. Figure 8 shows that increasing the voltage can result in a higher elongation value. When the travel rate and intensity rise, the elongation value decreases.

Table 9. Response table for Signal-to-Noise ratios for elongation value (larger is better).

Level	Travel Rate	Voltage	Intensity
1	34.43	33.83	34.85
2	34.13	34.72	33.71
Delta	0.30	0.89	1.13
Rank	3	2	1



(a)



Signal-to-noise: Larger is better

(b)

Figure 8. Taguchi analysis for elongation value: (a) Main Effects Plot for Means, and (b) SN ratios for Signal-to-Noise ratios (larger is better).

3.3. SEM Results

Figure 9 illustrates the SEM fracture surface of WAAM samples at different process parameters. The results point out the ductile fracture surface with dimples of the samples after the tensile test, indicating the high elasticity of the pieces [37–40]. Moreover, the fracture surface also reveals the equiaxial shape and grain size. For example, samples 4 and 10 with grain sizes $166 \mu\text{m}^2$ and $207 \mu\text{m}^2$ have larger dimple sizes. At the same time, samples 5 and 12, with grain sizes $62 \mu\text{m}^2$ and $79 \mu\text{m}^2$ have small dimple sizes. In addition, samples 6–12 with lower intensity ($U = 22\text{--}24 \text{ V}$, $I = 120 \text{ A}$) demonstrate mostly deeper dimples as they have more excellent ductility. Notably, some pores appear in Figure 9b,h,i, corresponding to samples 2, 8, and 9. These pores appear due to the shrinkage and emission of dissolved gas during solidification [41–43]. The supply of CO_2 gas during the WAAM process also contributes to the formation of pores.

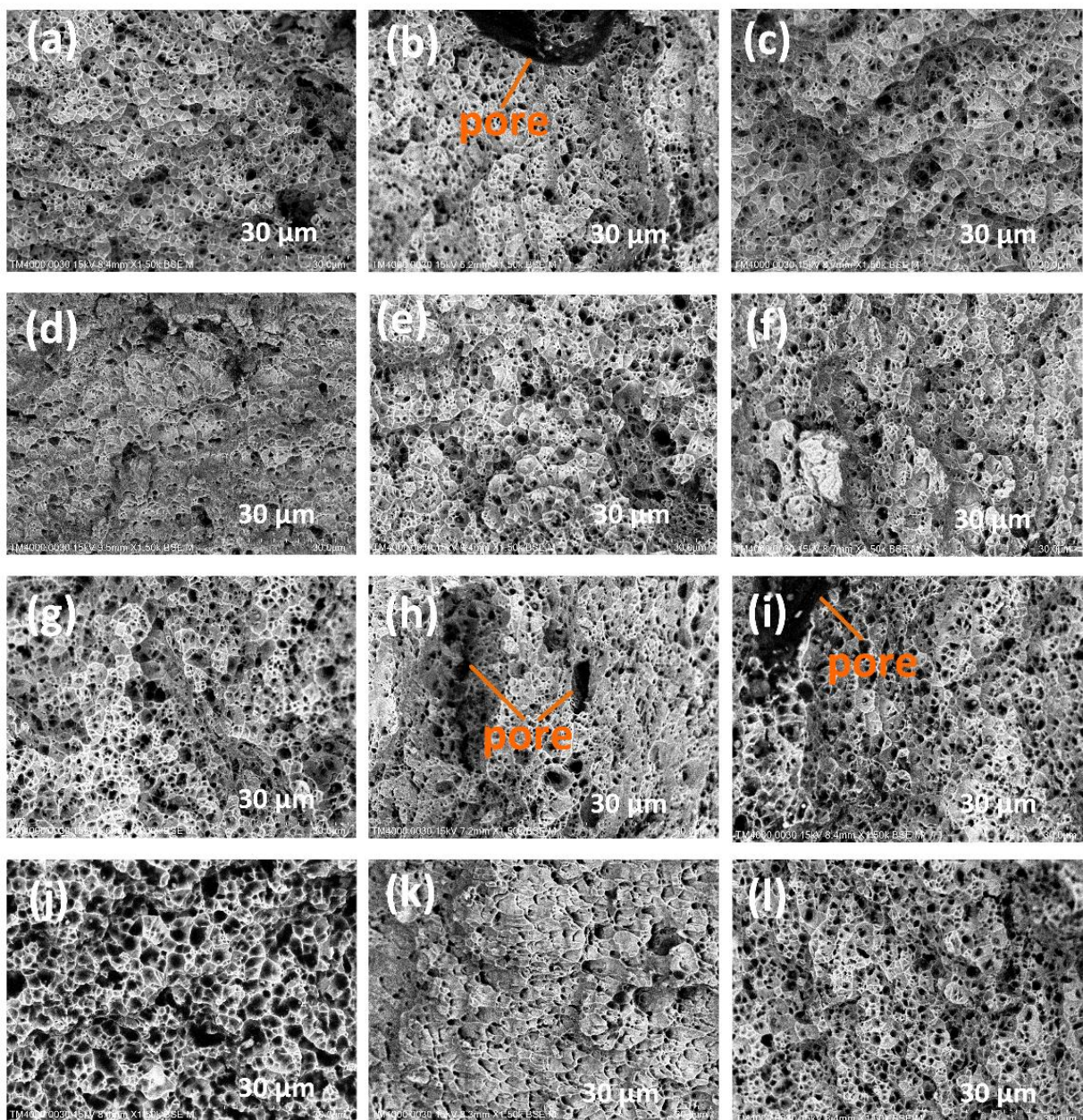


Figure 9. SEM fracture surface of WAAM samples at different process parameters: (a) sample 1, (b) sample 2, (c) sample 3, (d) sample 4, (e) sample 5, (f) sample 6, (g) sample 7, (h) sample 8, (i) sample 9, (j) sample 10, (k) sample 11, and (l) sample 12.

4. Conclusions

This study examines the microstructure and mechanical properties of low-carbon steel samples produced by the WAAM technique. The effects of travel rate, voltage, and intensity are investigated. The results show that the microstructure of the WAAM samples has an isotropy grain shape, with grain size number values varying from about 8–12. The smallest grain size area is $62 \mu\text{m}^2$, while the largest grain size is $207 \mu\text{m}^2$. Remarkably, the WAAM sample gains better mechanical properties with a higher UTS value and higher elongation at break value than the original wire. Compared to the original steel wire, the UTS value of the WAAM samples is 21–40% higher, varying from 599 MPa to 694 MPa. The sample that achieves the maximum UTS value of 694 MPa has a travel rate of $350 \text{ mm}\cdot\text{min}^{-1}$, a voltage of 24 V, and an electrical intensity of 120 A. The lowest UTS value, 599 MPa, is obtained by the WAAM sample with a travel rate of $400 \text{ mm}\cdot\text{min}^{-1}$, a voltage of 22 V, and an electrical intensity of 170 A. The elongation at break of the WAAM samples is also two or three times higher than the original wire, oscillating around 41–57%. The SEM results indicate the dimple shape of the fracture surface, resulting from a high-toughness fracture. Taguchi analyses show that factor travel rate is the most impact factor of the grain size. The voltage factor most impacts the UTS value, while the intensity factor most significantly impacts the elongation at break value.

Author Contributions: P.S.M., T.T.D. and V.-T.N.: Conceptualization, funding acquisition; V.-T.N., T.T.D. and M.-T.L.: writing original draft, investigation; H.V.T.N., T.T.D. and M.-T.L.: analyzing, visualization; T.M.T.U., P.S.M. and V.-T.N.: project administration; T.T.D., P.S.M. and M.-T.L.: investigation; V.T.T.N., P.S.M., M.-T.L. and V.-T.N.: writing, review, and editing. All authors have read and agreed to the published version of the manuscript.

Funding: This research received no external funding.

Institutional Review Board Statement: Not applicable.

Informed Consent Statement: Not applicable.

Data Availability Statement: The data used to support the findings of this study are available from the corresponding author upon request.

Acknowledgments: The authors acknowledge the support of HCMC University of Technology and Education for this study.

Conflicts of Interest: The authors declare no conflict of interest.

References

- Dilberoglu, U.M.; Gharehpapagh, B.; Yaman, U.; Dolen, M. The role of additive manufacturing in the era of industry 4.0. *Procedia Manuf.* **2017**, *11*, 545–554. [[CrossRef](#)]
- Gardan, J. Additive manufacturing technologies: State of the art and trends. *Int. J. Prod. Res.* **2016**, *54*, 3118–3132. [[CrossRef](#)]
- Gibson, I.; Rosen, D.; Stucker, B.; Khorasani, M.; Rosen, D.; Stucker, B.; Khorasani, M. *Additive Manufacturing Technologies*; Springer: Cham, Switzerland, 2021; Volume 17.
- Sing, S.L.; An, J.; Yeong, W.Y.; Wiria, F.E. Laser and electron-beam powder-bed additive manufacturing of metallic implants: A review on processes, materials and designs. *J. Orthop. Res.* **2016**, *34*, 369–385. [[CrossRef](#)]
- Murr, L.E.; Gaytan, S.M.; Ramirez, D.A.; Martinez, E.; Hernandez, J.; Amato, K.N.; Shindo, P.W.; Medina, F.R.; Wicker, R.B. Metal fabrication by additive manufacturing using laser and electron beam melting technologies. *J. Mater. Sci. Technol.* **2012**, *28*, 1–14. [[CrossRef](#)]
- Bhavar, V.; Kattire, P.; Patil, V.; Khot, S.; Gujar, K.; Singh, R. A review on powder bed fusion technology of metal additive manufacturing. In *Additive Manufacturing Handbook*; Taylor & Francis: Boca Raton, FL, USA, 2017; pp. 251–253.
- Singh, R.; Gupta, A.; Tripathi, O.; Srivastava, S.; Singh, B.; Awasthi, A.; Rajput, S.K.; Sonia, P.; Singhal, P.; Saxena, K.K. Powder bed fusion process in additive manufacturing: An overview. *Mater. Today Proc.* **2020**, *26*, 3058–3070. [[CrossRef](#)]
- Srivatsav, S.; Jayakumar, V.; Sathishkumar, M. Recent developments and challenges associated with wire arc additive manufacturing of Al alloy: A review. *Mater. Today Proc.* **2021**, *46*, 8561–8566. [[CrossRef](#)]
- Vishnukumar, M.; Pramod, R.; Kannan, A.R. Wire arc additive manufacturing for repairing aluminium structures in marine applications. *Mater. Lett.* **2021**, *299*, 130112. [[CrossRef](#)]
- Tomar, B.; Shiva, S.; Nath, T. A review on wire arc additive manufacturing: Processing parameters, defects, quality improvement and recent advances. *Mater. Today Commun.* **2022**, *31*, 103739. [[CrossRef](#)]

11. Singh, S.R.; Khanna, P. Wire arc additive manufacturing (WAAM): A new process to shape engineering materials. *Mater. Today Proc.* **2021**, *44*, 118–128. [[CrossRef](#)]
12. Treutler, K.; Wesling, V. The current state of research of wire arc additive manufacturing (WAAM): A review. *Appl. Sci.* **2021**, *11*, 8619. [[CrossRef](#)]
13. Dhinakaran, V.; Ajith, J.; Fahmidha, A.F.Y.; Jagadeesha, T.; Sathish, T.; Stalin, B. Wire Arc Additive Manufacturing (WAAM) process of nickel based superalloys—A review. *Mater. Today Proc.* **2020**, *21*, 920–925. [[CrossRef](#)]
14. Derekar, K.; Lawrence, J.; Melton, G.; Addison, A.; Zhang, X.; Xu, L. Influence of interpass temperature on wire arc additive manufacturing (WAAM) of aluminium alloy components. In *MATEC Web of Conferences*; EDP Sciences: Bali, Indonesia, 2019; Volume 269, p. 05001.
15. Singh, M.; Sharma, S.; Muniappan, A.; Pimenov, D.Y.; Wojciechowski, S.; Jha, K.; Dwivedi, S.P.; Li, C.; Królczyk, J.B.; Walczak, D.; et al. In Situ Micro-Observation of Surface Roughness and Fracture Mechanism in Metal Microforming of Thin Copper Sheets with Newly Developed Compact Testing Apparatus. *Materials* **2022**, *15*, 1368. [[CrossRef](#)]
16. Mehnen, J.; Ding, J.; Lockett, H.; Kazanas, P. Design study for wire and arc additive manufacture. *Int. J. Prod. Dev.* **2014**, *20*, 2–20. [[CrossRef](#)]
17. Busachi, A.; Erkoyuncu, J.; Colegrove, P.; Martina, F.; Watts, C.; Drake, R. A review of Additive Manufacturing technology and Cost Estimation techniques for the defence sector. *CIRP J. Manuf. Sci. Technol.* **2017**, *19*, 117–128. [[CrossRef](#)]
18. Singh, M.; Garg, H.K.; Maharana, S.; Yadav, A.; Singh, R.; Maharana, P.; Nguyen, T.V.T.; Yadav, S.; Loganathan, M.K. An Experimental Investigation on the Material Removal Rate and Surface Roughness of a Hybrid Aluminum Metal Matrix Composite (Al6061/SiC/Gr). *Metals* **2021**, *11*, 1449. [[CrossRef](#)]
19. Puzatova, A.; Shakor, P.; Laghi, V.; Dmitrieva, M. Large-Scale 3D Printing for Construction Application by Means of Robotic Arm and Gantry 3D Printer: A Review. *Buildings* **2022**, *12*, 2023. [[CrossRef](#)]
20. Huynh, T.T.; Nguyen, T.V.T.; Nguyen, Q.M.; Nguyen, K.T. Minimizing warpage for macro-size fused deposition modeling parts. *Comput. Mater. Contin.* **2021**, *68*, 2913–2923.
21. Prado-Cerqueira, J.L.; Diéguez, J.L.; Camacho, A.M. Preliminary development of a wire and arc additive manufacturing system (WAAM). *Procedia Manuf.* **2017**, *13*, 895–902. [[CrossRef](#)]
22. Wang, L.; Xue, J.; Wang, Q. Correlation between arc mode, microstructure, and mechanical properties during wire arc additive manufacturing of 316L stainless steel. *Mater. Sci. Eng. A* **2019**, *751*, 183–190. [[CrossRef](#)]
23. Luo, Y.; Li, J.; Xu, J.; Zhu, L.; Han, J.; Zhang, C. Influence of pulsed arc on the metal droplet deposited by projected transfer mode in wire-arc additive manufacturing. *J. Mater. Process. Technol.* **2018**, *259*, 353–360. [[CrossRef](#)]
24. Popov, V.V.; Fleisher, A. Hybrid additive manufacturing of steels and alloys. *Manuf. Rev.* **2020**, *7*, 6. [[CrossRef](#)]
25. Evans, S.I.; Wang, J.; Qin, J.; He, Y.; Shepherd, P.; Ding, J. A review of WAAM for steel construction—Manufacturing, material and geometric properties, design, and future directions. In *Structures*; Elsevier: Amsterdam, The Netherlands, 2022; Volume 44, pp. 1506–1522.
26. Martina, F.; Ding, J.; Williams, S.; Caballero, A.; Pardal, G.; Quintino, L. Tandem metal inert gas process for high productivity wire arc additive manufacturing in stainless steel. *Addit. Manuf.* **2019**, *25*, 545–550. [[CrossRef](#)]
27. Takagi, H.; Sasahara, H.; Abe, T.; Sannomiya, H.; Nishiyama, S.; Ohta, S.; Nakamura, K. Material-property evaluation of magnesium alloys fabricated using wire-and-arc-based additive manufacturing. *Addit. Manuf.* **2018**, *24*, 498–507. [[CrossRef](#)]
28. Shi, J.; Li, F.; Chen, S.; Zhao, Y.; Tian, H. Effect of in-process active cooling on forming quality and efficiency of tandem GMAW-based additive manufacturing. *Int. J. Adv. Manuf. Technol.* **2019**, *101*, 1349–1356. [[CrossRef](#)]
29. Yildiz, A.S.; Davut, K.; Koc, B.; Yilmaz, O. Wire arc additive manufacturing of high-strength low alloy steels: Study of process parameters and their influence on the bead geometry and mechanical characteristics. *Int. J. Adv. Manuf. Technol.* **2020**, *108*, 3391–3404. [[CrossRef](#)]
30. Xiong, J.; Li, Y.; Li, R.; Yin, Z. Influences of process parameters on surface roughness of multi-layer single-pass thin-walled parts in GMAW-based additive manufacturing. *J. Mater. Process. Technol.* **2018**, *252*, 128–136. [[CrossRef](#)]
31. Hosseini, V.; Höglström, M.; Hurtig, K.; Bermejo, M.A.V.; Stridh, L.-E.; Karlsson, L. Wire-arc additive manufacturing of a duplex stainless steel: Thermal cycle analysis and microstructure characterization. *Weld. World* **2019**, *63*, 975–987. [[CrossRef](#)]
32. Feng, Y.; Zhan, B.; He, J.; Wang, K. The double-wire feed and plasma arc additive manufacturing process for deposition in Cr-Ni stainless steel. *J. Mater. Process. Technol.* **2018**, *259*, 206–215. [[CrossRef](#)]
33. Tripathi, U.; Saini, N.; Mulik, R.S.; Mahapatra, M.M. Effect of build direction on the microstructure evolution and their mechanical properties using GTAW based wire arc additive manufacturing. *CIRP J. Manuf. Sci. Technol.* **2022**, *37*, 103–109. [[CrossRef](#)]
34. Abd Razak, N.A.; Ng, S.S. Investigation of effects of MIG welding on corrosion behaviour of AISI 1010 carbon steel. *J. Mech. Eng. Sci.* **2014**, *7*, 1168–1178. [[CrossRef](#)]
35. Sayed, A.R.; Kumar, D.; Shahare, G.M.; Nawkhare, N.N.; Bhanarkar, R.Y.; Dhande, D.R.; Ramteke, A.R.; Bharadkar, U.M. Mechanical and microstructural testing of C-45 material welded by using SMAW and GMAW process. *Mater. Today Proc.* **2021**, *38*, 223–228. [[CrossRef](#)]
36. Tawfik, M.M.; Nemat-Alla, M.M.; Dewidar, M.M. Effect of travel speed on the properties of Al-Mg aluminum alloy fabricated by wire arc additive manufacturing. *J. Mater. Eng. Perform.* **2021**, *30*, 7762–7769. [[CrossRef](#)]

37. Nagasai, B.P.; Malarvizhi, S.; Balasubramanian, V. Effect of welding processes on mechanical and metallurgical characteristics of carbon steel cylindrical components made by wire arc additive manufacturing (WAAM) technique. *CIRP J. Manuf. Sci. Technol.* **2022**, *36*, 100–116. [[CrossRef](#)]
38. Gisario, A.; Kazarian, M.; Martina, F.; Mehrpouya, M. Metal additive manufacturing in the commercial aviation industry: A review. *J. Manuf. Syst.* **2019**, *53*, 124–149. [[CrossRef](#)]
39. Minh, P.S.; Nguyen, V.-T.; Nguyen, V.T.; Uyen, T.M.T.; Do, T.T.; Nguyen, V.T.T. Study on the Fatigue Strength of Welding Line in Injection Molding Products under Different Tensile Conditions. *Micromachines* **2022**, *13*, 1890. [[CrossRef](#)] [[PubMed](#)]
40. Buchanan, C.; Gardner, L. Metal 3D printing in construction: A review of methods, research, applications, opportunities and challenges. *Eng. Struct.* **2019**, *180*, 332–348. [[CrossRef](#)]
41. Yousefian, P.; Tiryakioğlu, M. Pore formation during solidification of aluminum: Reconciliation of experimental observations, modeling assumptions, and classical nucleation theory. *Metall. Mater. Trans. A* **2018**, *49*, 563–575. [[CrossRef](#)]
42. Gu, J.; Yang, S.; Gao, M.; Bai, J.; Zhai, Y.; Ding, J. Micropore evolution in additively manufactured aluminum alloys under heat treatment and inter-layer rolling. *Mater. Des.* **2020**, *186*, 108288. [[CrossRef](#)]
43. Uyen, T.M.T.; Minh, P.S.; Nguyen, V.-T.; Do, T.T.; Nguyen, V.T.; Le, M.-T.; Nguyen, V.T.T. Trajectory Strategy Effects on the Material Characteristics in the WAAM Technique. *Micromachines* **2023**, *14*, 827. [[CrossRef](#)]

Disclaimer/Publisher’s Note: The statements, opinions and data contained in all publications are solely those of the individual author(s) and contributor(s) and not of MDPI and/or the editor(s). MDPI and/or the editor(s) disclaim responsibility for any injury to people or property resulting from any ideas, methods, instructions or products referred to in the content.